IEEE Access
Multidisciplinary | Rapid Review | Open Access Journal

Received August 19, 2021, accepted October 30, 2021, date of publication November 8, 2021, date of current version November 19, 2021.

Digital Object Identifier 10.1109/ACCESS.2021.3126785

Using Communication Channel Equalization to Remove Atmospheric Turbulence in Star Signal Detection

DAVID SHIUNG[1], (Member, IEEE), YA-YIN YANG[2], AND WEN-LONG CHIN[3], (Senior Member, IEEE)

[1]Department of Electronics Engineering, National Changhua University of Education, Changhua City 500, Taiwan
[2]Department of Electrical Engineering, National Cheng Kung University, Tainan City 701, Taiwan
[3]Department of Engineering Science, National Cheng Kung University, Tainan City 701, Taiwan

Corresponding author: Ya-Yin Yang (ivyyang64@gmail.com)

This work was supported by the Taiwan Ministry of Science and Technology under Grant MOST-110-2221-E-018-008.

ABSTRACT In this paper, we explore the problem of removing atmospheric turbulence to obtain better images of remote sidereal star systems. The imaging process is remodeled as a transmit–receive wireless communication paradigm in a novel approach for correcting space- and time-varying blur in stellar images. In particular, the effect of starlight passing through atmospheric turbulence is modeled as multipath fading communication channels. The problem is then transformed into channel equalization in space and time domains to produce a sharp stellar image. This approach involves first estimating the center of a blurred stellar image. Next, linear regression obtains an equivalent two-dimensional channel response through decomposition of the blurred image into the weighted sum of the diffraction-limited patterns in the spatial domain. Finally, an alignment algorithm is implemented for synthesis, and a final output is generated. Experiments were performed with real field-captured images; the results revealed that this approach could be used to effectively correct image blur and obtain diffraction-limited stellar images.

INDEX TERMS Atmospheric turbulence, full-width at half maximum (FWHM), linear regression, point spread function (PSF).

I. INTRODUCTION

Atmospheric turbulence poses a challenge for long-distance imaging. Imaging through the atmosphere can be substantially affected by turbulence, in which air temperature, density, and index of refraction vary [1]– [3]. The initial plane of the wavefront can become distorted, and the value of the refractive index changes along a ray at different points on the wavefront. This phenomenon causes image quality degradation and has been a problem for deep space optical communication [4], remote sensing [5], [6], astronomical observation [1], [2], [7], and natural imaging [8], [9] since the 1950s. Recorded images may be marred by geometric distortion, space- and time-varying blur, or loss of resolution and sensitivity [3], [9].

Such problems with atmospheric turbulence can be avoided by using space-based imaging systems, such as the Hubble space telescope (HST). However, these systems are costly ($2 billion) and, in the case of telescopes larger than the HST, infeasible [3], [10]. Space-based telescopes cost approximately $100,000 per minute of use; thus, any effort to improve image quality constitutes a relatively inexpensive solution [11]. Some solutions have been proposed for reducing the effects of atmospheric turbulence on the image resolution and sensitivity of imaging systems. Adaptive optics (AO) is a hardware-based approach [1]– [3]. AO systems improve image quality by sensing the waveform deformation of a reference star near a target object and then deforming one or more deformable mirrors to compensate for poor image focus. A valuable measure of AO system effectiveness is the Strehl ratio, which is defined as the ratio of the intensity of a point source to that produced by a perfectly diffraction-limited telescope of the same aperture and throughput [3]. An AO system has a maximum theoretical Strehl ratio of 1.0 and can achieve a ratio of 0.5 in practice [3]. Another parameter for quantifying the impact of atmospheric turbulence on image quality is the full width at half maximum (FWHM) of a point source [3], [12]. The degree of dispersion of the light spot is referred to as astronomical seeing and is typically in the range of a few arcseconds [13].

The associate editor coordinating the review of this manuscript and approving it for publication was Qilian Liang.

Another commonly used approach for imaging through atmospheric turbulence is so-called lucky imaging [14]– [16]. In this approach, fusion methods are applied to selected short exposures in which the instantaneous wavefront distortion over the telescope aperture is negligible. The probability of obtaining a usable short-exposure image can be approximated as $Prob \cong exp[-0.1557(d/r_0)^2]$ for $d/r_0 \geq 3.5$ [17], where d is the telescope aperture diameter and r_0 is the Fried coherence length of the distorted waveform defined in [18]. However, this probability decreases rapidly with d. For example, for an acceptable good-image probability of 10^{-6}, a maximum increase in diameter of $10r_0$ is permissible [17]. Under favorable astronomical seeing conditions, lucky imaging can capture near-diffraction-limited images, whereas under poor astronomical seeing conditions, the FWHM can be improved up to fourfold [15].

The use of signal processing techniques to remove atmospheric turbulence has been a popular approach for obtaining high quality images for decades (e.g., [7], [9], [11], [19], [20], and [21] and the references therein). An observed image $R(\mathbf{x})$ on a two-dimensional (2D) focal plane of spatial coordinate $\mathbf{x}$ can be modeled as follows [9], [20]:

$$R(\mathbf{x}) = (T \otimes \phi \otimes h_{\mathbf{x}})(\mathbf{x}) + W(\mathbf{x}), \tag{1}$$

where $\otimes$ is a 2D convolutional operator; T and W are perfect images unaffected by the atmosphere and by sensor noise, respectively; $h_{\mathbf{x}}$ is a space-varying and time-varying (turbulence-induced) point spread function (PSF) at the focal plane location $\mathbf{x}$; ϕ is a space-invariant diffraction-limited PSF determined by the shape of the telescope aperture, wavelength, and focal ratio of the telescope; $h_{\mathbf{x}}$ and ϕ are patch-wise models; and R, T, and W are frame-wise models. The ultimate goal of these methods is to restore the perfect image T. T is typically obtained by deconvolving R with the composite PSF $\phi \otimes h_{\mathbf{x}}$. However, this problem is not well-posed (in that the inverse matrix does not exist) and is chaotic (a small change in W causes a significant variation in inversion). Moreover, this approach breaks the physical law of diffraction because the recovered image is not affected by the physical dimensions of the telescope optics. We may even conclude that a smartphone camera could obtain the same image T as an observatory telescope. Clearly, this conclusion is incorrect. Image quality is typically evaluated by assessing whether the recovered image is sharper than the unprocessed image. However, within the astronomical community, this approach is considered ineffective for removing atmospheric turbulence. Although some images processed through deconvolution appear visually shaper than the original images, these methods often induce artifacts in the processed image and provide limited useful scientific information [7], [22]. Thus, astronomers usually adopt hardware-based solutions such as the HST or AO systems to overcome poor astronomical seeing.

Aiming to obtain a diffraction-limited image (i.e., an image limited in resolution only by diffraction laws), we attempted to restore $T \otimes \phi$ to improve imaging by removing atmospheric turbulence. Our solution was to remodel (1) as a communication channel equalization problem and propose a new framework that could be considered a software-based version of AO; we then apply this framework to restore high-quality images of a remote sidereal star and of the multiple star system Epsilon Lyrae captured with atmospheric turbulence. The reconstructed stellar images were evaluated regarding the diffraction limit of telescope optics and the ground truth images. We also compared our results with the method of online blind deconvolution in [21] (OBD), which also attempted to recover T. Specifically, we propose a communication engineering model for the detection of star signals in space through atmosphere.

Our previous work presented at the 2016 Asia Pacific Wireless Communications Symposium [12] introduced techniques for estimating the degree of atmospheric turbulence in terms of a target star's FWHM through digital signal processing. Both theoretical Gauss and Kolmogorov PSFs of field-captured stellar images were compared, and the results indicated that the Kolmogorov PSF method had better fit with the field images. In our research presented at the 2018 International Symposium on Personal, Indoor and Mobile Radio Communications [23], we studied the parallels between wireless communication and astronomical observation. Extending [23], we present a theoretical basis for obtaining the equivalent channel response of a target star as well as a framework for image restoration. We defined a rotation-based autocorrelation function for classifying a target star into a single-star or multiple-star system. Finally, we validated the approach with two experiments (one on Beta Leonis and the other on Epsilon Lyrae). These results, presented in this paper, are all novel.

Our contributions to solving the problems associated with the removal of atmospheric turbulence to better detect cosmic signals are summarized below.

A. INTRODUCTION OF CHANNEL EQUALIZATION TECHNIQUES FOR THE DETECTION OF A REMOTE STELLAR IMAGE

We achieve this goal by transforming cosmic signal detection models into a communication engineering model. In the model, a remote sidereal star is regarded as a 2D delta signal, and the receiver consists of a ground-based telescope situated in front of a camera sensor. The atmospheric turbulence between the star and receiver is represented as multipath fading channels that perturb the ideal 2D delta signal into a stellar speckle. The undistorted cosmic signal is detected as long as the channel is equalized. This model is detailed in Section II.

B. DEVELOPMENT OF A 2D CHANNEL EQUALIZER TO RECONSTRUCT A STELLAR IMAGE

A blurred stellar speckle is decomposed into a weighted sum of basis functions, which are condensed into one function with an appropriate intensity. The derivations are presented in Section III, and the equalizer's performance in terms of

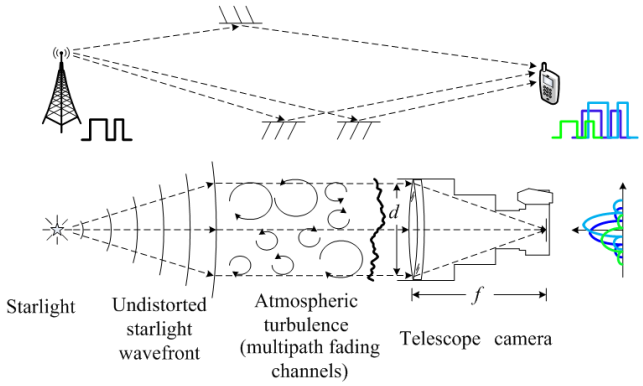

FIGURE 1. Parallels between wireless communication (top) and cosmic signal detection (bottom) with atmospheric turbulence [23].

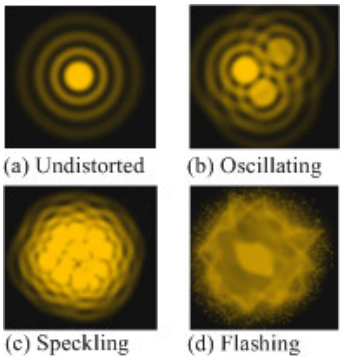

FIGURE 2. Examples of a 2D impulse signal detected through atmospheric turbulence channels [13].

the FWHM is provided in Section IV. The conclusions are presented in Section V.

II. COMMUNICATION ENGINEERING MODELING

The parallels between starlight reception and wireless communication are illustrated in Fig. 1. Consider a remote sidereal star that is almost infinitely far from the Earth. This target star is regarded as the impulse signal, and its wavefront (cophase waveform) is essentially planar. The top part of Fig. 1 depicts a digital communication over multipath channels, and the bottom part depicts an astronomical observation. The light spot on a camera sensor accumulates of overlapping diffraction patterns with varying amplitudes and spatial coordinates. This accumulation is affected by atmospheric turbulence with cells of various sizes and refractive index values. The telescope and its camera sensor behind it are a receiver in this generalized wireless communication system. The telescope diameter is d, and its focal plane is situated behind the lens at a distance f. Because the camera sensor outputs numerous discrete pixels, the receiving parts are equivalent to a digital baseband receiver. A camera mounted on the equator could monitor Earth's rotation such that no relative motion can be observed between the camera and the target sidereal star. We assume that the focus of the image is accurate and that no loss of optical features occurs. Image blur is caused by atmospheric turbulence and telescope diffraction. In our approach, the light from a star is regarded as the transmitter, and the atmosphere is regarded as multipath fading channels. The receiver is the optical telescope on the ground, which captures blurred stellar images through the atmosphere. The blurred image from the camera sensor can be equalized through a 2D channel to produce a sharp image.

A. PERFECT DIFFRACTION AND BLURRED PATTERNS

The telescopic image of a point source is its diffraction pattern caused by the shape of the telescope lens aperture. The undistorted diffraction pattern of a point of starlight passing through a circular telescope lens is depicted in Fig. 2(a). As the telescope aperture increases, the central light spot (Airy disk) and its surrounding diffraction rings become increasingly narrow. Thus, a high spatial resolution can be achieved. However, in field experiments, the recorded starlight is suboptimal because of the influence of atmospheric turbulence. Figs. 2(b) and 2(c) display images distorted by low-altitude and high-altitude atmospheric turbulence, respectively. The image slowly deviates from its average position with a deflection angle of several arcseconds [13]. In both cases, the recorded images reflect the accumulation of several undistorted diffraction patterns. The image recorded during observation reflects the accumulation of fast-moving undistorted diffraction patterns. The distorted image displayed in Fig. 2(d) is the result of a point source passing through a section of turbulent cells with large diffraction index values. This phenomenon is referred to as flashing and indicates the accumulation of more diffraction patterns.

The relative intensity (normalized to 1.0 at the center of the PSF) for a circular aperture is [24]

$$\phi(|\mathbf{x}|) = \left[\frac{2J_1(k|\mathbf{x}|)}{k|\mathbf{x}|}\right]^2, \tag{2}$$

where $|\mathbf{x}| = \sqrt{x^2+y^2}$ is the radial distance in the focal plane from (x, y) to the center of the Airy disk and $k = \frac{\pi d}{\lambda f}$. λ is the waveform of monochromatic radiation, and $J_n(\cdot)$ is the first-kind Bessel function of order n. Fig. 3 presents the normalized intensity [i.e., (2)] along the normalized distance $k|\mathbf{x}|$. The Rayleigh limit (distance from the center of the Airy disk to the first minimum) is $3.83k|\mathbf{x}|$. According to a numerical simulation, the FWHM for the ideal diffraction pattern is

$$FWHM_{IDL} = 3.24k|\mathbf{x}|. \tag{3}$$

The structure of the ideal PSF in (Fig. 3) indicates that only a fraction of the total energy is confined to the Airy disk. The encircled energy function (EEF) surrounded by a ring of radius $|\mathbf{x}|$ and normalized to 1.0 when $|\mathbf{x}|$ approaches infinity—can be represented as [24]

$$EEF(|\mathbf{x}|) = 1 - {J_0}^2(k|\mathbf{x}|) - {J_1}^2(k|\mathbf{x}|). \tag{4}$$

Equation (4) is plotted in Fig. 4 and can be used to estimate the encircled energy of a truncated ideal diffraction pattern.

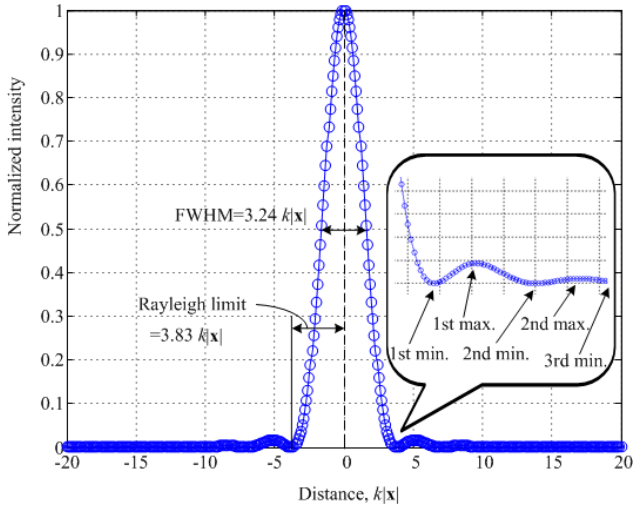

FIGURE 3. FWHM and Rayleigh limit for a perfect PSF of circular aperture.

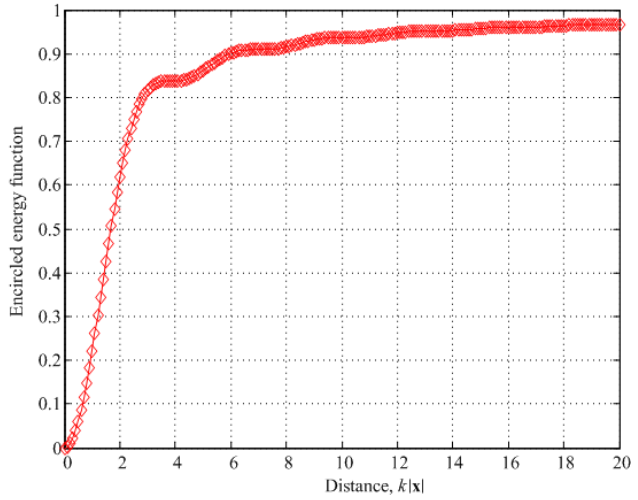

FIGURE 4. Plot of the EEF as a function of distance $k|\mathbf{x}|$.

The use of the truncated pattern as a basis function for decomposing diffused starlight is detailed in Section III.

B. ASTRONOMICAL CHANNEL

The frequency of variation in astronomical seeing is no more than 15 Hz. Consequently, the telescopic image slowly deviates from its average position with a deflection angle of several arcseconds [4], [13]. Therefore, if the sidereal starlight from an image sensor is integrated for more than 1 s, quasi-Gaussian function can approximate the accumulated images. Both the Gauss and Kolmogorov distribution functions are commonly used to represent a blurred image [22]. These functions are referred to as the Gauss and Kolmogorov PSFs for simplicity.

The Gauss and Kolmogorov PSFs (normalized to 1.0 at the center of the PSF) can be written as follows [22]:

$$f_{GAS}(x, y) = e^{-\frac{x^2+y^2}{2\sigma^2}}, \quad -\infty < x,\ y < \infty \tag{5}$$

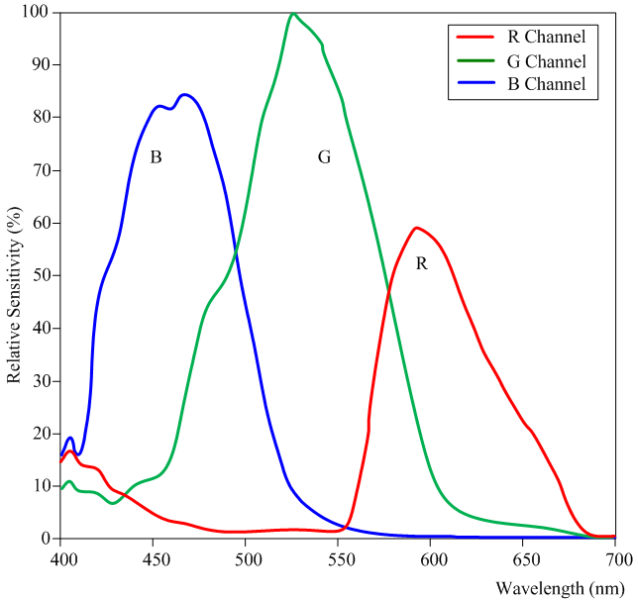

FIGURE 5. Efficiency of the receiver at various wavelengths.

and

$$f_{KOL}(x, y) = e^{-\frac{|x|^{\frac{5}{3}}+|y|^{\frac{5}{3}}}{\sigma}}, \quad -\infty < x,\ y < \infty, \tag{6}$$

respectively. The FWHM for each of the two PSFs depends on the coefficient σ and is unrelated to the absolute image strength. A quantitative representation of the FWHM was provided in [12].

C. STELLAR IMAGE FROM A CAMERA SENSOR

The camera sensor comprises an array of pixels of pixel length p. Each pixel has three channels [i.e., red–green–blue (RGB) color channels] that can capture starlight at different frequency bands. Thus, the camera sensor can be regarded as a set of data sites scattered across a spatial grid.

Fig. 5 presents an example of the relative sensitivity to the three color channels of a camera sensor. Although each color channel can sense a range of wavelengths, we let $\lambda_R = 656.2$ nm, $\lambda_G = 550$ nm, and $\lambda_B = 450$ nm represent the wavelengths of the R, G, and B channels, respectively. Thus, a diffused stellar image can be decomposed into a weighted sum of diffraction patterns with their centers scattered around the centroid of the target star image.

D. PROBLEM FORMULATION

Consider the problem of recovering a diffraction-limited image $T \otimes \phi$ from a sequence of N observed (blurry and noisy, with no nebulosity or saturated pixels) stellar images R_n, where $n = 1, \cdots, N$. By (1), we define the nth observed image $R_n(\mathbf{x})$ as

$$R_n(\mathbf{x}) = \left(T \otimes \phi \otimes h_{\mathbf{x},n}\right)(\mathbf{x}) + W_n(\mathbf{x}), \tag{7}$$

where $h_{\mathbf{x},n}$ and W_n represent turbulence-induced PSF and the sensor noise of the nth image, respectively. The assumptions for the problem are as follows: (i) we have no prior or partial information regarding the "true" unknown image T, (ii) the space-time-varying PSF $h_{\mathbf{x},n}$ is unknown, (iii) the sensor noise W_n is also unknown, (iv) the space-invariant diffraction-limited PSF ϕ is known, and (v) all the images R_n, T, W_n, and the PSF $h_{\mathbf{x},n}$ are nonnegative.

Sections III and IV describe the processes of spatial channel equalization and performance evaluation, respectively.

III. IMPLEMENTATION OF SPATIAL CHANNEL EQUALIZATION

First, a target star[1] is selected from a stellar image for spatial channel equalization. For notational convenience, the target star is aligned with the focal plane's coordinates (0, 0). However, the derivations described herein can easily be applied to cases in which the target star is not centered at (0, 0). We also omit the subscript n for R_n, $h_{\mathbf{x},n}$, and W_n.

To reconstruct the original image, the blurred stellar image must be resolved into a sum of perfectly diffracted patterns (i.e., basis functions with centers scattered around the centroid). Each basis function is a duplicate of a diffraction pattern in the spatial domain that has been shifted by the length of a certain number of pixels to produce a perfect diffraction pattern. The process of perfect image reconstruction is formulated as a linear regression problem; the set of coefficients $\{w_l\}_{l=1,\cdots,L}$ for $P_\phi(\mathbf{x})$ over the observation sites $\{\mathbf{x}_m\}_{m=1,\cdots,M}$ can approximate the target star in $R(\mathbf{x})$:

$$R(\mathbf{x}) \cong P_\phi(\mathbf{x}) = \sum_{l=1}^{L} w_l \phi_l(\mathbf{x}) = \sum_{l=1}^{L} w_l \phi(\mathbf{x} - \mathbf{x}_l) \tag{8}$$

constrained by

$$|\mathbf{x}_l| \le \epsilon, \quad l = 1, \cdots, L \tag{9}$$

and

$$\|\mathbf{e}\|^2 = \mathbf{e}^t\mathbf{e} \text{ is minimized.} \tag{10}$$

L is the number of resolvable multipaths for a displacement of deflection ϵ on the focal plane. The basis function $\phi_l(\mathbf{x})$ is a shifted duplicate of the basis function $\phi(\mathbf{x})$ with its center placed at $\mathbf{x}_l$; that is, $\phi_l(\mathbf{x}) = \phi(\mathbf{x} - \mathbf{x}_l)$. The error vector $\mathbf{e}$ is defined as the difference between $R(\mathbf{x})$ and $P_\phi(\mathbf{x})$: $\mathbf{e} = [R(\mathbf{x}_1) - P_\phi(\mathbf{x}_1), \cdots, R(\mathbf{x}_M) - P_\phi(\mathbf{x}_M)]^t$. In general, $M \ge L$.

Fig. 6 presents the algorithm for restoring the image of the target star. First, the color stellar image is decomposed into RGB subchannels to remove noise, and the centroid of each subchannel is estimated. The coefficients $\{w_l\}_{l=1,\cdots,L}$ for each subchannel are obtained as the channel response for all N stellar images. The coefficients $\{w_l\}_{l=1,\cdots,L}$ are determined by linear regression; the channel responses for the sequence of stellar images are then aligned and averaged with respect to the centroid. The averaged channel responses are used to determine if the image is of a single-star or a multiple-star system. Finally, the images of the three subchannels are reconstructed and synthesized to obtain a final color image.

[1]Here, the target star may be a single-star or a multiple-star system appearing as a single point of light.

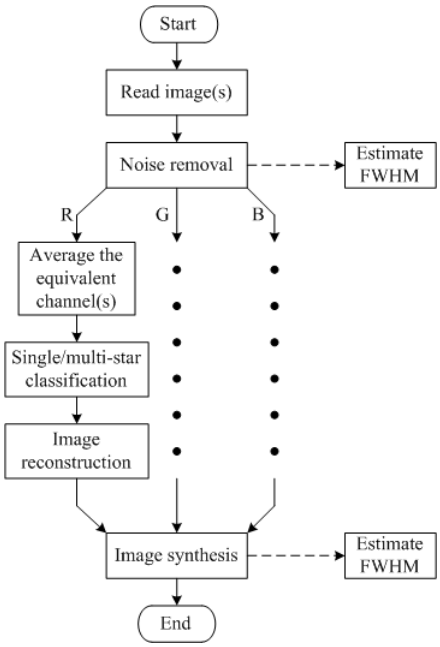

FIGURE 6. Algorithm for restoring the target star.

A. LEAST SQUARES APPROXIMATION

Substituting the M observation sites into (8) yields

$$\begin{cases} R(\mathbf{x}_1) = w_1\phi_1(\mathbf{x}_1) + \cdots + w_L\phi_L(\mathbf{x}_1) + e_1, \\ R(\mathbf{x}_2) = w_1\phi_1(\mathbf{x}_2) + \cdots + w_L\phi_L(\mathbf{x}_2) + e_2, \\ \qquad\qquad \vdots \\ R(\mathbf{x}_M) = w_1\phi_1(\mathbf{x}_M) + \cdots + w_L\phi_L(\mathbf{x}_M) + e_M. \end{cases} \tag{11}$$

The system of equations in (11) can be rewritten as

$$\mathbf{A}\mathbf{w} + \mathbf{e} = \mathbf{r}, \tag{12}$$

where

$$\mathbf{A} = \begin{bmatrix} \phi_1(\mathbf{x}_1) & \phi_2(\mathbf{x}_1) & \cdots & \phi_L(\mathbf{x}_1) \\ \phi_1(\mathbf{x}_2) & \phi_2(\mathbf{x}_2) & \cdots & \phi_L(\mathbf{x}_2) \\ \vdots & \vdots & & \vdots \\ \phi_1(\mathbf{x}_M) & \phi_2(\mathbf{x}_M) & \cdots & \phi_L(\mathbf{x}_M) \end{bmatrix},$$

$\mathbf{w} = [w_1, w_2, \cdots, w_L]^t$, $\mathbf{e} = [e_1, e_2, \cdots, e_M]^t$, and $\mathbf{r} = [R(\mathbf{x}_1), R(\mathbf{x}_2), \cdots, R(\mathbf{x}_M)]^t$. To obtain the optimal solution $\hat{\mathbf{w}}$ for the weighting vector $\mathbf{w}$, the least squares rule is applied to $\|\mathbf{e}\|^2 = \mathbf{e}^t\mathbf{e}$, and $\nabla\left(\|\mathbf{e}\|^2\right) = 0$. This yields the following equation [25]:

$$\begin{aligned} \nabla\left(\|\mathbf{e}\|^2\right) &= \nabla\left((\mathbf{A}\mathbf{w} - \mathbf{r})^t(\mathbf{A}\mathbf{w} - \mathbf{r})\right) \\ &= \nabla\left((\mathbf{w}^t\mathbf{A}^t - \mathbf{r}^t)(\mathbf{A}\mathbf{w} - \mathbf{r})\right) \\ &= 2\mathbf{A}^t\mathbf{A}\mathbf{w} - 2\mathbf{A}^t\mathbf{r} = 0. \end{aligned} \tag{13}$$

The solution is

$$\hat{\mathbf{w}} = (\mathbf{A}^t\mathbf{A})^{-1}\mathbf{A}^t\mathbf{r} \tag{14}$$

if the matrix $\mathbf{A}^t\mathbf{A}$ is nonsingular. Because $\mathbf{A}$ is an $M \times L$ matrix, where $M \geq L$, $\mathbf{A}^t\mathbf{A}$ is an $L \times L$ matrix.

B. PROOF OF WELL-POSEDNESS

Let $\mathbf{Q} = \mathbf{A}^t\mathbf{A}$. If $\mathbf{Q}$ is nonsingular, then $\mathbf{Q}^{-1}$ exists and the equations (8)–(10) are well-posed (i.e., a solution exists and we have a unique solution).

A consideration of positive-definite matrices aids in formulating the proof. A real symmetric matrix $\mathbf{Q}$ is regarded as semipositive definite if its associated quadratic form is nonnegative—in other words, if

$$\mathbf{c}^t\mathbf{Q}\mathbf{c} = \sum_{i=1}^{L}\sum_{j=1}^{L} c_i c_j Q_{ij} \geq 0 \tag{15}$$

for all $\mathbf{c} = [c_1, \cdots, c_L]^t \in \mathbb{R}^L$. $\mathbb{R}$ denotes the set of real numbers, and Q_{ij} is the element of $\mathbf{Q}$ in the ith row and jth column. If the quadratic form (15) is 0 only for $\mathbf{c} = \mathbf{0}$, then $\mathbf{Q}$ is positive definite. A crucial property of positive-definite matrices is that all their eigenvalues are positive; thus, they are nonsingular [26].

According to the definitions of $\mathbf{A}$ and the basis function $\phi(|\mathbf{x}|)$ in (2), $\mathbf{Q}$ is real. Furthermore,

$$\mathbf{Q}^t = \left(\mathbf{A}^t\mathbf{A}\right)^t = \mathbf{A}^t(\mathbf{A}^t)^t = \mathbf{A}^t\mathbf{A} = \mathbf{Q}. \tag{16}$$

Thus, $\mathbf{Q}$ is also symmetric. Therefore, $\mathbf{Q}$ is positive definite because the quadratic form defined in (15) becomes

$$\begin{aligned}\mathbf{c}^t\mathbf{Q}\mathbf{c} &= \mathbf{c}^t\mathbf{A}^t\mathbf{A}\mathbf{c} \\ &= \mathbf{c}^t\begin{bmatrix} \sum_{i=1}^{M}\phi_1^2(\mathbf{x}_i) & \cdots & \sum_{i=1}^{M}\phi_1(\mathbf{x}_i)\phi_L(\mathbf{x}_i) \\ \vdots & \ddots & \vdots \\ \sum_{i=1}^{M}\phi_L(\mathbf{x}_i)\phi_1(\mathbf{x}_i) & \cdots & \sum_{i=1}^{M}\phi_L^2(\mathbf{x}_i) \end{bmatrix}\mathbf{c} \\ &= \sum_{i=1}^{M}[c_1\phi_1(\mathbf{x}_i) + \cdots + c_L\phi_L(\mathbf{x}_i)]^2 \geq 0. \end{aligned} \tag{17}$$

Notably, the equality holds only for $\mathbf{c} = \mathbf{0}$, indicating that the solution in (14) exists and is unique for the least squares approximation.

C. IMPLEMENTATION

Consider a rectangular camera sensor used to capture images of a target star with atmospheric turbulence. The camera sensor consists of an array of pixels with size p. In this scenario, the centers of the basis functions coincide with the centers of the pixels in the pixel array. Moreover, the observation sites are located at the centers of the pixels in the pixel array; however, the observation sites should fully cover the space occupied by the diffused target star. In addition, the number of basis functions must be sufficient to account for deflections of starlight traveling through atmospheric turbulence.

Because the gray level recorded with the camera sensor is discrete and because a pixel can only capture starlight within a confined space, the basis function $\phi(\mathbf{x})$ in (2) must first be transformed into its discrete version $\phi[m, n]$ at the mth horizontal pixel and nth vertical pixel, where m and n are integers. Thus, $\phi[m, n]$ is a matrix and can be represented as follows:

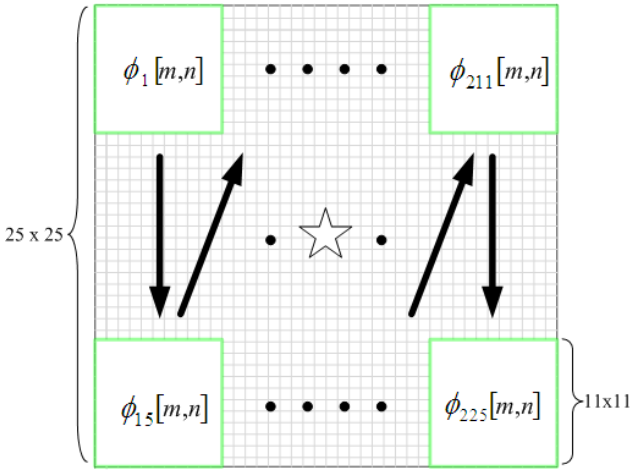

FIGURE 7. Pixel array for representing basis functions.

$$\phi[m, n] = \int_{(m-\frac{1}{2})p}^{(m+\frac{1}{2})p}\int_{(n-\frac{1}{2})p}^{(n+\frac{1}{2})p}\phi(x, y)dxdy, \tag{18}$$

where $m, n \in \mathbb{Z}$. The number of pixels required to represent $\phi[m, n]$ is determined by the percentage of the power ratio intended to be preserved with respect to the total power contained in $\phi(\mathbf{x})$. However, for any given number of pixels, the contained power is also a function of the physical dimensions of the telescope, the pixel size of the camera sensor, and the considered wavelength. The same technique used to obtain $\phi_l(\mathbf{x})$ and $R(\mathbf{x})$ is used to obtain the discrete counterparts $\phi_l[m, n]$ and $R[m, n]$, respectively.

Fig. 7 presents an example of a pixel array for representing basis functions for $d = 115$ mm, $f = 845.25$ mm, $p = 6.4236$ μm, $\lambda = 656.2$ nm, and $\epsilon = 5.5p$, yielding $k = 6.5137 \times 10^5$ m^{-1}. As indicated in (5) and (6), both the Gauss and Kolmogorov PSFs extend to infinity and decay as x and y approach infinity. If we take $M = 25^2$ as the number of observation sites, then $L = 15^2$. By (4), we confirm that the 11×11 matrix for $\phi[m, n]$ contains approximately 97.21% of the total energy. The basis functions are shifted replicas of the basis function at the various locations presented in Fig. 7. The approximation defined in (8) is then rewritten as follows:

$$R[m, n] \cong \sum_{l=1}^{L} w_l\phi_l[m, n]. \tag{19}$$

The performance of the spatial channel equalizer was evaluated by calculating the FWHM values for the imaged star at each of the three subchannels. Both Gauss and Kolmogorov PSFs achieved adequate fit with starlight images. However, according to [12], the Kolmogorov PSF achieves better fit for field-captured stellar images than the Gauss PSF does. The

FWHM obtained from fitting with a Kolmogorov PSF can be represented in terms of the parameter σ as follows:

$$FWHM_{KOL} = 2\sigma(\ln 2)^{\frac{3}{5}}. \tag{20}$$

Notably, σ determines the shape of the PSF and has the same units as $FWHM_{KOL}$. Thus, the problem of estimating the FWHM of a single star is transformed into a surface-fitting problem with respect to σ.

D. SINGLE-STAR VERSUS MULTIPLE-STAR SYSTEMS

A multiple-star system has two or more component stars orbiting around their center of mass. Understanding the type of the target star, for example, a single star or multiple stars, is essential for reconstructing the diffraction-limit stellar image. This information can be obtained by analyzing the channel response of the target star by using (14) and then using a rotation-based autocorrelation function for the channel response defined as

$$A(\theta) \triangleq \sum_{n,m} \langle \hat{\mathbf{w}} \rangle_{N,\measuredangle 0} \circledast \langle \hat{\mathbf{w}} \rangle_{N,\measuredangle \theta}, \tag{21}$$

where θ is an integer multiple of 90°. Note the matrix operator $\langle \cdot \rangle_{N,\measuredangle\theta}$ denotes averaging N images and then rotating counterclockwise with respect to the center of mass by θ degrees. The notation $\circledast$ indicates the element-wise in-place product of the two matrices.

Using (21), we can classify whether a target star is a single star or a multiple-star system. The channel response for a single star is circularly symmetric, whereas that of a multiple-star system is asymmetric. Fig. 8 compares the normalized autocorrelation functions, $A(\theta)/A(0)$, for a single star (SAO 67323) and a binary star (Epsilon Lyrae 2). A binary star consists of two stars orbiting around their center of mass and is of concern to astronomers due to the interesting physical phenomena that they exhibit [27]. We can see that the SAO 67323 image has almost identical autocorrelation for all the three RGB subchannels due to its circularly symmetric channel response. By contrast, the shape of the channel response for the Epsilon Lyrae 2 image is more elliptical. Thus, the normalized autocorrelation is 1 when $\theta = 0°, 180°$ and is reduced when $\theta = 90°$ and 270°.

Our 2D channel equalization approach is based on the decomposition of a diffused stellar image into a linear combination of perfect diffraction patterns and then aligning the centroids of the patterns. If the target star is classified as a single star, the reconstructed image is obtained by shifting each response to its centroid with a strength equal to the sum of its channel responses. If the target star is classified as a multiple-star system, the channel response is first surface fitted by two Gaussian distribution functions to estimate the centroids of the two component stars. This process can be continued to identify a third or fourth component star. In Section IV, we provide more detailed examples demonstrating the utility of this approach for analyzing binary stars and compare the method with OBD.

TABLE 1. Parameters used in experiments 1 and 2.

	Experiment 1	Experiment 2
Target	Beta Leonis	Epsilon Lyrae
Classification	Single star	Multiple-star system
Scope diameter, d (mm)	115	115
Focal length, f (mm)	845.25	845.25
Pixel size, p (μm)	6.4236	6.4236
ϵ	$5.5p$	$5.5p$
Exposure time (sec.)	1	1
M	$25^2(=625)$	$25^2(=625)$
L	$15^2(=225)$	$15^2(=225)$
λ_R (nm)	656.2	656.2
λ_G (nm)	550	550
λ_B (nm)	450	450

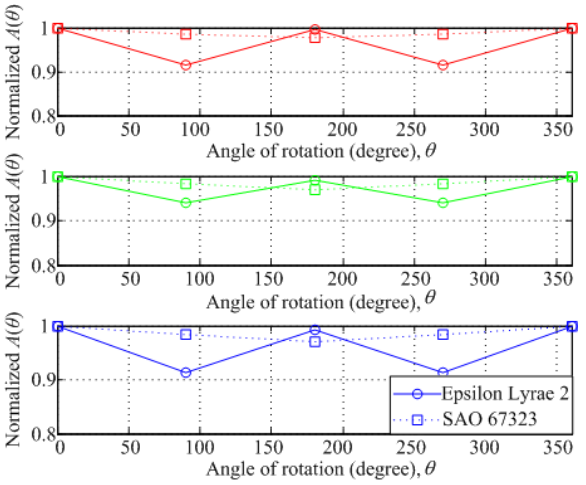

FIGURE 8. A comparison of the autocorrelation functions for a single star (SAO 67323) and a binary star (Epsilon Lyrae 2) in RGB subchannels (from top to bottom).

IV. PERFORMANCE EVALUATION

We present the results of our method on two types of actual astronomical images. All images were taken by the authors using an off-the-shelf 4.5-inch f/7.35 APM/TMB CNC LWII refractor and a Canon EOS 350D digital single lens reflex (DSLR) camera on Mount He-Huan in Kun-Yang, Taiwan. The first data set (Experiment 1) comprised single-shot images of Beta Leonis, a blue-white star of magnitude 2.23 and 36 light years from Earth. The second data set (Experiment 2) comprised a sequence of images of Epsilon Lyrae, a multiple star system that consists of at least two binary stars. The northern and southern binary pairs are named Epsilon 1 and Epsilon 2, respectively. The parameters used are tabulated in Table 1.

A. SINGLE-STAR SYSTEM

Fig. 9 presents the original stellar image captured through atmospheric turbulence. The camera sensor has relative sensitivity in the wavelength range of 400–700 nm, as presented in Fig. 5. The color images were linearly combined with identical weights (i.e., 1/3) for each color channel. We observed that the original stellar image was not sharp and had large FWHM values. We use (3) and (20) to estimate the FWHM values of the three color channels; the results are displayed

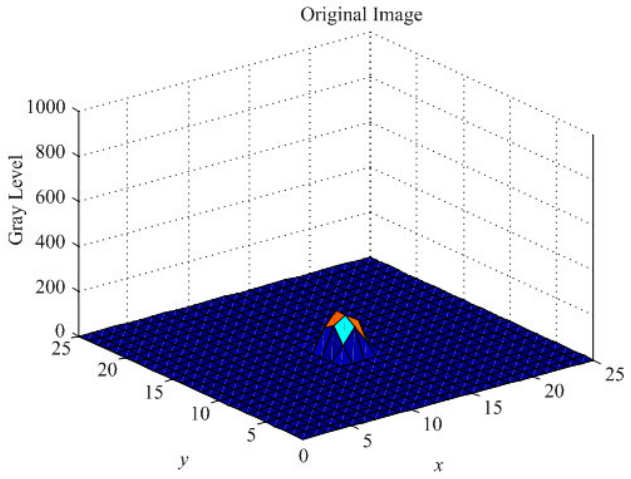

FIGURE 9. Original stellar image.

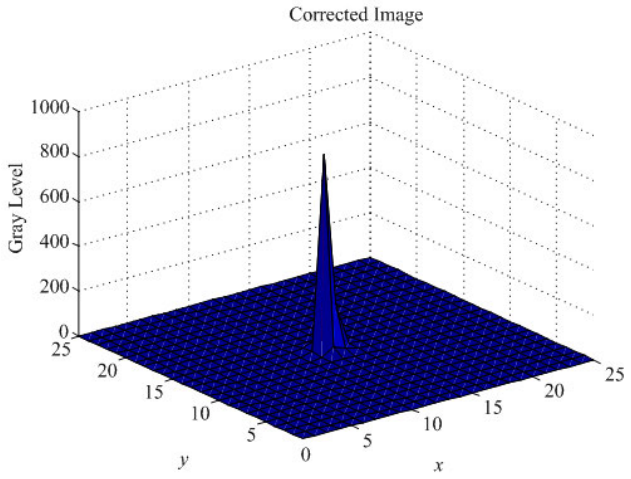

FIGURE 10. Corrected image.

TABLE 2. Improvement in FWHMs before and after channel equalization.

Image	Before	After	Theoretical Limit
R (656.2 nm)	3.2532 arcsec	1.2581 arcsec	1.2111 arcsec
G (550 nm)	3.7708 arcsec	1.2581 arcsec	1.0151 arcsec
B (450 nm)	3.1827 arcsec	1.2581 arcsec	0.8305 arcsec
Synthesized	3.4059 arcsec	1.2581 arcsec	0.9977 arcsec

in Table 2. The FWHM values of the three color channels ranged from 3.1827 arcsec for the B channel to 3.7708 arcsec for the G channel. The RGB synthesized stellar image had an FWHM value of 3.4059 arcsec.

The reconstructed stellar image is thus identical to an image with a perfect diffraction pattern at an appropriate intensity. After the replicas of each channel were aligned in the spatial domain, all three channels achieved the same FWHM of 1.2581 arcsec. The FWHM derived for the synthesized stellar image was unchanged. The resulting synthesized color image is displayed in Fig. 10. The corrected stellar image was sharper than the original image and had a significantly smaller FWHM. Our results are similar to those reported for corrected images processed with AO in other studies, such as [1]–[3]. The results after equalization are summarized in Table 2.

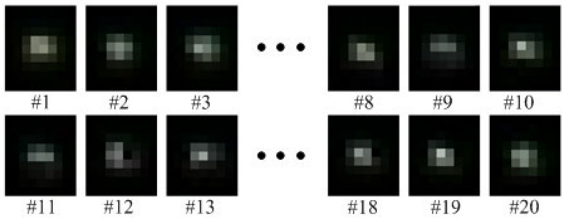

FIGURE 11. Temporal evolution of 20 observed images of the binary star system Epsilon Lyrae 1.

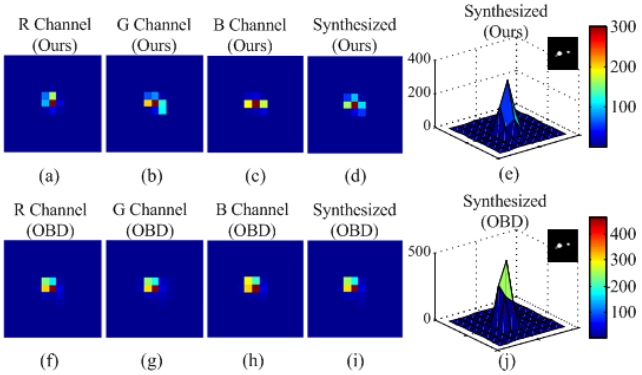

FIGURE 12. Comparison of the restored images of Epsilon Lyrae 1 with our approach (top row) and with OBD (bottom row). The ground truth images are included at the upper-right corners of (e) and (j).

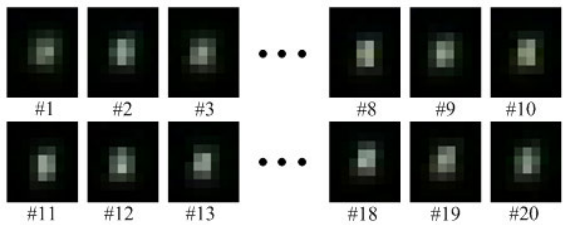

FIGURE 13. Temporal evolution of 20 observed images of the binary star system Epsilon Lyrae 2.

Table 2 also lists the theoretical limits for a scenario with infinitesimal pixels. The R channel came closest to the theoretical limit, followed by the G and B channels. The synthesized stellar image was 26.1% $[(1.2581 - 0.9977)/0.9977 \times 100\%]$ wider than the theoretical limit. The FWHM could be improved for all channels if a camera sensor with a smaller pixel size is used.

B. MULTIPLE-STAR SYSTEM

In Experiment 2, we use images of Epsilon Lyrae to demonstrate image recovery and analysis for a multiple-star system. Epsilon Lyrae[2] has two notable binary stars named Epsilon Lyrae 1 and Epsilon Lyrae 2. The component stars of Epsilon Lyrae 1 have magnitudes of 4.7 and 6.2 and are separated by 2.6 arcsec. The main components of Epsilon Lyrae 2 have magnitudes 5.1 and 5.5 and are separated by 2.3 arcsec. According to Table 1, the resolution of the sensor array was $p/f = 1.5675$ arcsec. Furthermore, as indicated in Table 2,

[2]The fifth component of this system, orbiting Epsilon Lyrae 2, has a maximum observed separation of 0.2 arcsec and is below the resolution limit of our imaging platform.

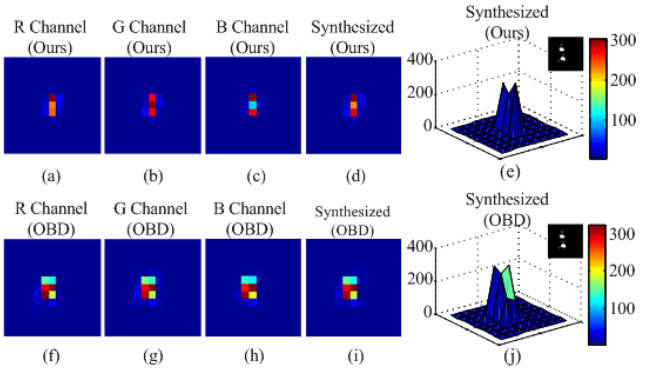

FIGURE 14. Comparison of the restored images of Epsilon Lyrae 2 with our approach (top row) and with OBD (bottom row). The ground truth images are included at the upper-right corners of (e) and (j).

the resolution limits of the optics were at least 1.2111 arcsec. Thus, Epsilon Lyrae 1 & 2 were ideal targets for testing the spatial resolution capabilities of our algorithm.

Fig. 11 and 13 present a series of 20 observed images of Epsilon Lyrae 1 and 2. Comparisons of our approach with OBD [21] for Epsilon Lyrae 1 and 2 are displayed in Fig. 12 and 14, respectively. These images are best viewed on a screen rather than in print. The restored images are presented in Fig. 12(a)–(e) and Fig. 14(a)–(e); those from OBD are displayed in Fig. 12(f)–(j) and Fig. 14(f)–(j). The ground truth images of these two binary stars are provided in the upper-right corners of subfigures (e) and (f). For Epsilon Lyrae 1, our approach generates comparable or slightly better-defined images than OBD does. Both our approach and OBD were unable to reveal distinguishable component stars in this case. However, by using (21) to identify the shape of the autocorrelation function, we can conclude that the target star is indeed a binary star and that the two component stars have a magnitude difference of 1.25 and are separated by 2.0 arcsec. The restored images in Figs. 12 and 14 recovered $T \otimes h$, whereas that of OBD recovered T only. Thus, the proposed method is useful for analyzing a multiple-star system even if the multiple-star system is visually indistinguishable from a single star.

Fig. 14 clearly demonstrates that both our approach and that of OBD can both resolve the two component stars of Epsilon Lyrae 2. However, our approach resolves the two component stars better than OBD. The restored image also better identifies the correct placement of the two components than OBD does as revealed by comparison with the ground truth image. Through numerical calculation, we verify that the two component stars have a magnitude difference of 0.24 and are separated by 2.12 arcsec. These results demonstrate the utility of our approach for analyzing multiple-star systems.

V. CONCLUSION AND FUTURE WORK

We proposed and demonstrated a novel approach based on wireless communication methods for restoring blurred stellar images. First, the centers of the RGB channels in a blurred image of a target star were estimated; subsequently, linear regression was applied to estimate the RGB channel response in the spatial domain to in turn approximate the image with a weighted sum of independent basis functions. Finally, the blurred image was equalized and reconstructed in the spatial domain to obtain a sharp image. Detections of both single-star (Beta Leonis) and multiple-star systems (Epsilon Lyrae) were demonstrated. Numerical results revealed that the FWHM of the reconstructed image could be significantly improved to approach the theoretical diffraction limit. This technique extends stellar imaging by using wireless communication methods and is a new approach to imaging through atmospheric turbulence.

Future work includes investigating equalization of star images containing nebulosity with space-varying PSFs. This equalization might be achieved by dividing the image into sections with stars and with nebulosity and applying different techniques to the sections.

REFERENCES

[1] R. K. Tyson, *Principles of Adaptive Optics*, 4th ed. Boca Raton, FL, USA: CRC Press, 2016.
[2] J. W. Hardy, *Adaptive Optics for Astronomical Telescopes*, 1st ed. Oxford, U.K.: Oxford Univ. Press, 1998.
[3] P. Hickson. (Jun. 2008). *Fundamentals of Atmospheric and Adaptive Optics*. [Online]. Available: http://www.aeos.ulg.ac.be/upload/ao.pdf
[4] H. Hemmati, *Deep Space Optical Communications*, 1st ed. Pasadena, CA, USA: Jet Propulsion Laboratory, 2005.
[5] X.-L. Zhao, F. Wang, T.-Z. Huang, M. K. Ng, and R. J. Plemmons, "Deblurring and sparse unmixing for hyperspectral images," *IEEE Trans. Geosci. Remote Sens.*, vol. 51, no. 7, pp. 4045–4058, Jul. 2013.
[6] X. Qiang, T. Liu, S. Feng, F. Zong, M. Wu, J. Chang, and J. Zhao, "Remote sensing of atmospheric turbulence profiles by laser guide stars," in *Proc. 29th Int. Laser Radar Conf. (ILRC)*, Hefei, China, Jun. 2017, p. 06014.
[7] R. Berry and J. Burnell, *The Handbook of Astronomical Imaging Processing*, 2nd ed. Richmond, VA, USA: Willmann-Bell, 2005.
[8] M. S. Hosseini and K. N. Plataniotis, "Convolutional deblurring for natural imaging," *IEEE Trans. Image Process.*, vol. 29, pp. 250–264, 2020.
[9] X. Zhu and P. Milanfar, "Removing atmospheric turbulence via space-invariant deconvolution," *IEEE Trans. Pattern Anal. Mach. Intell.*, vol. 35, no. 1, pp. 157–170, Jan. 2013.
[10] NASA. (Nov. 2020). *Hubble Space Telescope*. [Online]. Available: https://hubblesite.org/
[11] R. Molina, J. Nunez, F. J. Cortijo, and J. Mateos, "Image restoration in astronomy: A Bayesian perspective," *IEEE Signal Process. Mag.*, vol. 18, no. 2, pp. 11–29, Mar. 2001.
[12] D. Shiung, Y.-Y. Yang, C.-S. Yang, and J.-S. Liou, "Estimate the astronomical seeing by using digital signal processing," in *Proc. 13rd IEEE Veh. Technol. Soc. Asia Pacific Wireless Commun. Symp. (VTS APWCS)*, Tokyo, Japan, Aug. 2016, pp. 69–73.
[13] Black Oak Observatory. (Nov. 2013). *Astronomical Seeing—Part I: The Nature of Turbulence*. [Online]. Available: https://www.handprint.com/ASTRO/seeing1.html
[14] S. Zhang, J. Zhao, and J. Wang, "An efficient lucky imaging system for astronomical image restoration," in *Proc. 12nd Adv. Maui Opt. Space Surveill. Technol. Conf. (AMOS)*, Maui, HI, USA, Sep. 2011, pp. 754–761.
[15] N. M. Law, C. D. Mackay, and J. E. Baldwin, "Lucky imaging: High angular resolution imaging in the visible from the ground," *Astron. Astrophys.*, vol. 446, no. 2, pp. 739–745, Feb. 2006.
[16] J. Wang, B. Li, and K. Xing, "A new real-time lucky imaging algorithm and its implementation techniques," *IEEE Access*, vol. 8, pp. 52192–53308, 2020.
[17] D. L. Fried, "Probability of getting a lucky short-exposure image through turbulence," *J. Opt. SoC. Amer.*, vol. 68, no. 12, pp. 1651–1658, Dec. 1978.
[18] D. L. Fried, "Optical heterodyne detection of an atmospherically distorted signal wave front," *Proc. IEEE*, vol. 55, no. 1, pp. 57–67, Jan. 1967.

[19] M. Hirsch, S. Sra, B. Scholkopf, and S. Harmeling, "Efficient filter flow for space-variant multiframe blind deconvolution," in *Proc. IEEE Comput. SoC. Conf. Comput. Vis. Pattern Recognit.*, San Francisco, CA, USA, Jun. 2010, pp. 607–614.
[20] S. Harmeling, M. Hirsch, S. Sra, and B. Scholkopf, "Online blind deconvolution for astronomical imaging," in *Proc. IEEE Int. Conf. Comput. Photography (ICCP)*, San Francisco, CA, USA, Apr. 2009, pp. 1–7.
[21] M. Hirsch, S. Harmeling, S. Sra, and B. Schölkopf, "Online multi-frame blind deconvolution with super-resolution and saturation correction," *Astron. Astrophys.*, vol. 531, p. A9, Jul. 2011.
[22] W.-H. Wang, *Advanced Wide-Field Astrophotography*, 3rd ed. Fengyuan, Taiwan: Starworks, 2019.
[23] D. Shiung, P.-H. Hsieh, and Y.-Y. Yang, "Parallels between wireless communication and astronomical observation," in *Proc. IEEE 29th Annu. Int. Symp. Pers., Indoor Mobile Radio Commun. (PIMRC)*, Bologna, Italy, Sep. 2018, pp. 1–6.
[24] R. R. Shannon and J. C. Wyant, *Applied Optics and Optical Engineering*, vol. 9, 1st ed. New York, NY, USA: Academic, 1983, ch. 4.
[25] S. H. Friedberg, A. J. Insel, and L. E. Spence, *Linear Algebra*, 5th ed. London, U.K.: Pearson, 2019.
[26] G. E. Fasshauer, *Meshfree Approximation Methods With MATLAB*, 1st ed. Singapore: World Scientific, 2007.
[27] H. Karttunen, P. Kröger, H. Oja, M. Poutanen, and K. J. Donner, *Fundamental Astronomy*, 6th ed. Berlin, Germany: Springer, 2017.

DAVID SHIUNG (Member, IEEE) received the B.S. degree from the National Tsing Hua University, Hsinchu, Taiwan, in 1995, and the M.S. and Ph.D. degrees from the National Taiwan University, Taipei City, Taiwan, in 1997 and 2002, respectively, all in electrical engineering. He designed communication ASICs at Novatek and Mediatek Semiconductor Corporation, Hsinchu, from 2002 to 2007. From 2007 to 2008, he was a Postdoctoral Researcher at the Institute of Communication Engineering, National Taiwan University. He is currently an Associate Professor with the Institute of Communication Engineering, National Changhua University of Education, Changhua City, Taiwan. His research interests include signal processing for wireless communication and astronomical imaging. He served as a Guest Editor for the Special Section on Green Signal Processing for Wireless Communications and Networking of IEEE Access.

YA-YIN YANG received the Ph.D. degree in electrical engineering from the National Taiwan University, Taiwan, in 2009. She is currently an Assistant Researcher with the Institute of Computer and Communication Engineering, National Cheng Kung University, Tainan City, Taiwan. Her research interests include channel estimation, radio resource allocation, and interference cancellation for wireless communication systems.

WEN-LONG CHIN (Senior Member, IEEE) received the B.S. and Ph.D. degrees in electronics engineering from the National Chiao Tung University, Hsinchu, Taiwan, and the M.S. degree in electrical engineering from the National Taiwan University, Taipei City, Taiwan. He is currently a Professor with the Department of Engineering Science, National Cheng Kung University. Before holding the faculty position, he worked at Hsinchu Science Park, Taiwan, for over 11 years, leading communication and network ASIC designs. His research interests include ASIC design and DSP for communications and networking. He served as an Associate Editor for IEEE Access and *EURASIP Journal on Wireless Communications and Networking*. He currently serves as a Technical Editor for IEEE Wireless Communications.